ARTICLE

Field-Induced slow magnetic relaxation and luminescence thermometry in a mononuclear ytterbium complex

Received 00th January 20xx,
Accepted 00th January 20xx

DOI: 10.1039/x0xx00000x

Matilde Fondo,[a,*] Julio Corredoira-Vázquez,[a] Ana M. García Deibe,[a] Jesús Sanmartín Matalobos,[a] Martín Amoza,[a] Alexandre M. P. Botas,[b] Rute A. S. Ferreira,[b] Luís D. Carlos, [b,*] Enrique Colacio[c]

The mononuclear complex [Yb($H_3L^{1,1,4}$)]·2MeOH (**1**·2MeOH), with a new heptadentate N_4O_3 ligand, was isolated and structurally characterised. The opto-magnetic properties of **1**·2MeOH were investigated, showing that this complex is a bifunctional compound. Accordingly, **1**·2MeOH reveals two coexisting functionalities: field-induced single molecule magnet behaviour, and Yb^{3+}-centred NIR fluorescence dependent on temperature (25-300 K). The magnetic relaxation in this pentagonal bipyramidal complex does not seem to be of the Orbach type, and this is supported by the discrepancy between the anisotropic energy barrier found by fitting the magnetic data to an Orbach model and by spectroscopic studies. Ab initio calculations further validate the magnetic relaxation mechanisms and spectroscopic results.

Introduction

Multifunctional molecular materials belong to a class of compounds that combine several physical or chemical properties into a single molecule. Among different multifunctional systems, a particular emphasis has been made to design magnetic molecular materials with additional capabilities.[1] In this way, the field of molecular magnetism took a turn in its direction with the discovery of the first single ion magnet (SIM) in 2003,[2] the bis-phtalocyanine terbium complex [Tb(Pc_2)], and, accordingly, the demonstration that lanthanoid (Ln) ions can show slow relaxation of the magnetization. Besides, trivalent lanthanoid ions (Ln^{3+})-based complexes present specific luminescence that covers a large spectral range, from the visible to the near-infrared (NIR), with some exceptional features ascribed to the intra-4f transitions, such as characteristic narrow line-like emissions (<4 nm), long lifetimes (10^{-6}-10^{-3} s), or usually high luminescence quantum yields (>80%).[3] Despite these advantageous properties of Ln^{3+} ions, and a relatively quick growth of reported Ln^{3+}-based SMMs,[4-7] the number of these compounds spectroscopically studied is still relatively small.[8-9] Accordingly, the first work reporting the coexistence of slow relaxation of the magnetization and Ln^{3+}-based luminescence was published in 2009.[10] In the same way, the earliest publication correlating relaxation dynamics and light emission dates from 2012,[11] while an inductive effect between the magnetic field and luminescence has only been demonstrated in 2016.[12] Therefore, bi-functional molecular-based materials merging luminescence with magnetic properties have been the target of increasing interest. The potential applications of lanthanoid-based magneto-luminescent complexes include manufacture of molecular spintronics devices, single molecule detection or quantum read-out.

Among lanthanoid ions, Dy^{3+} is the most used one to design luminescent SMMs.[8-9] This seems to be due to its Kramers nature, its high *S* and *J* values, its oblate character of the electronic density, and its emission in the visible region of the electronic spectrum. The second most investigated f-ion in magnetic-luminescent materials is Yb^{3+}, but, despite this, few examples of mononuclear Yb single ion magnets (SIMs) were spectroscopically analysed.[8-9,15-19] Besides, in none of these cases, the temperature dependence of the luminescence properties was determined, although this analysis can be useful in the search for optical sensors for temperature measurements. Recently, a dinuclear ytterbium compound was reported as the first field-induced Yb-SMM luminescent thermometer[20] but, as far as we know, no mononuclear Yb SIMs were described to act also as luminescent temperature sensors. With these considerations in mind, and following with our study on the coordination chemistry of lanthanoid ions with polydentate N,O donors and their magnetic analysis,[21] we decided to study the opto-magnetic properties of a mononuclear Yb complex of a novel heptadentate ligand, and the results achieved are described herein.

Results and discussion

Synthesis

[Yb($H_3L^{1,1,4}$)]·2MeOH (**1**·2MeOH) was obtained by a modification of a previously reported method,[22] as summarised in Scheme 1. Thus, mixing of $Yb(OAc)_3$ with the mixture of the products obtained in the

[a] *Departamento de Química Inorgánica, Facultade de Química, Universidade de Santiago de Compostela, Campus Vida, 15782 Santiago de Compostela, Spain.*
[b] *Phantom-g, CICECO – Aveiro Institute of Materials, Department of Physics, University of Aveiro, 3810-193 – Aveiro, Portugal*
[c] *Departamento de Química Inorgánica, Facultad de Ciencias, Universidad de Granada, Avda Fuentenueva s/n, 18071 Granada, Spain.*

Electronic Supplementary Information (ESI) available: Figures S1-S10 and Tables S1-S8. CCDC. 2006553 For ESI and crystallographic data in CIF format see DOI: 10.1039/x0xx00000x

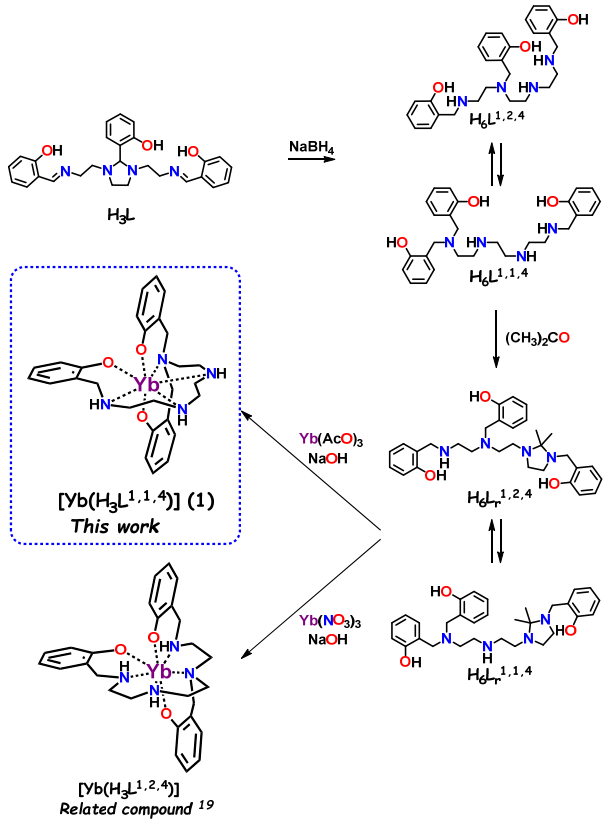

Scheme 1. Reaction scheme for isolation of **1**·2MeOH and related [Yb($H_3L^{1,2,4}$)].[22]

reduction of H_3L with $NaBH_4$ in a methanolic basic medium (NaOH) leads to the formation of copious single crystals of **1**·2MeOH and, therefore, this sample has been obtained with high purity. The isolation of this complex containing the $[H_3L^{1,1,4}]^{3-}$ ligand is quite unexpected, as the published synthesis,[22] where the reaction conditions are very similar, led to isolate [Yb($H_3L^{1,2,4}$)] (Scheme 1). Nevertheless, the difference between both compounds can be explained by the different basicity of the medium. In our case study, the operational pH of the reaction medium is higher, given that ytterbium(III) acetate is used instead of the ytterbium(III) nitrate employed in the related synthesis. Thus, this finding is in agreement with the aforementioned results,[22] where the equilibrium between $H_6L^{1,2,4}$ and $H_6L^{1,1,4}$ is reported to be displaced towards the $H_6L^{1,1,4}$ species with increasing pH of the medium, and this shows the high versatility of this chemistry.

In addition, the stability of **1**·2MeOH was checked by thermogravimetric analysis (TGA). The thermogram of the complex (Fig. S1) shows that it loses the methanol solvate between 23 and 160 ºC but that the sample is thermally stable up to 292ºC, where it begins to decompose.

Crystal structure of 1·2MeOH

The asymmetric unit of **1**·2MeOH comprises two molecules of the neutral complex [Yb($H_3L^{1,1,4}$)], in addition to methanol as solvate. This latter one is chiral, as the three consecutive protonated amine N atoms of the coordinated ligand are asymmetric. In addition to these two complex units, with (*R*,*S*,*R*) and (*S*,*R*,*S*) configurations, henceforth called **1**.1 and **1**.2, respectively (see caption of Fig. 1), two solvated methanol molecules are interacting with each complex molecule.

An ellipsoid diagram of one of the enantiomorphs of **1** is shown in Fig. 1, while selected distances and angles are listed in Table S1. As commented above, both (*R*,*S*,*R*) and (*S*,*R*,*S*) enantiomers are present in the asymmetric unit, so the crystal is racemic, but a Flack parameter[23] was calculated (Table S2), as this orthorhombic crystal structure belongs to the acentric *Pca*2_1 group, and to the *mm*2 crystal class. Although this class is not chiral or enantiomorphic, it presents a polar axis direction (*z*), which means that the unit-cell origin may be arbitrarily placed along this axis.[24] In acentric crystals, this Flack parameter determines a correct absolute structure and a closely coincident orientation of the structure concerning this polar axis, but in contrast with homochiral crystals, not the enantiopurity or racemic twinning evaluation. The presence of both (*R*,*S*,*R*) and (*S*,*R*,*S*) enantiomers in the asymmetric unit indicates their crystallographic non-equivalence, although both complex units are chemically equal. In fact, their distances and angles are totally comparable (Table S1), so this aspect does not deserve further discussion, although the short intermolecular Yb···Yb distance of 7.285(1) Å is rather noticeable.

In both crystallographically non-equivalent [Yb($H_3L^{1,1,4}$)] molecules, the trianionic amine-phenol ligand $[H_3L^{1,1,4}]^{3-}$ acts as heptadentate, with all its nitrogen and oxygen atoms coordinated to the metal centre. This leads to an N_4O_3 environment around the Yb^{III} ions, where the phenolic oxygen atoms OX1 and OX2 (X = 1 or 2 for **1**.1 or **1**.2, respectively) occupy the apical sites of the distorted pentagonal bipyramid. Many of the geometric parameters for this bipyramid,

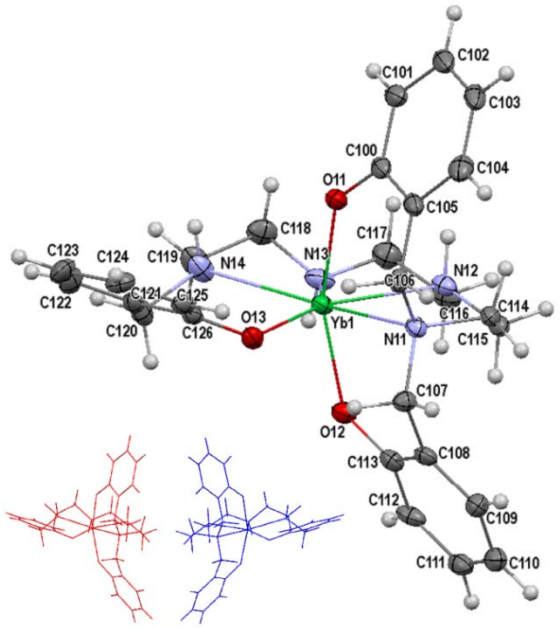

Fig. 1. Ellipsoid diagram (40% probability) of the (*R*,*S*,*R*) enantiomer (**1**.1) of [Yb($H_3L^{1,1,4}$)] present in the asymmetric unit of **1**·2MeOH. Its labelling scheme displays numbers starting with 1, whereas equivalently, that of the other enantiomer (**1**.2) starts with 2. The **1**.1 moiety (red unit) contains three asymmetric N atoms (N12, N13, N14) with configurations *R*, *S*, and *R*, respectively, and consequently, N22, N23, and N24 of unit **1**.2 (blue unit) display *S*, *R* and *S* configurations, correspondingly. Additionally, a sticks representation of both enantiomers is shown (bottom left) to illustrate the chirality of the compound.

which are listed in Table S1, are also similar to those reported for [Yb($H_3L^{1,2,4}$)],[22] although some differences deserve to be mentioned. Thus, the axial O-Yb-O angle of the bipyramid is wider in related [Yb($H_3L^{1,2,4}$)] (169.4(1)º *vs ca.* 160º for **1**.1 and **1**.2). Furthermore, the angles between consecutive donors in the plane are closer to the ideal 72 ° in the [Yb($H_3L^{1,2,4}$)] complex, indicating that the presence of two arms bonded to the same nitrogen atom, as it occurs in **1**, leads to a higher distortion of the pentagonal bipyramidal geometry. This geometry for **1**.1 and **1**.2, according to the SHAPE program (Table S3),[25] is distorted towards a capped trigonal prism. The distortion is also supported by the degree of deviation of the N_4O equatorial plane from the mean calculated plane. Accordingly, for **1**.1, the maximum deviation of any atom from the least square calculated plane is *ca*. 0.691 Å, while for **1**.2 is *ca*. 0.373 Å, and both calculated planes form an angle of 50.05 °.

Besides, it should be mentioned that there are no intramolecular hydrogen bonds in **1**, but a double intermolecular contact, via $O_{methanol}$-H···O_{phenol} and N_{amine}-H···$O_{methanol}$ bonds, exists between each solvated methanol molecule and a coordinated ligand. Furthermore, C-H···π and N-H···π interactions, mostly propagated in the *b* direction, collaborate on the crystal packing.

Moreover, the comparison of the experimental powder X-ray diffractogram of the crystalline product **1**·2MeOH with the calculated one from single X-ray diffraction data (Fig. S2) demonstrates that the product has been obtained with high purity, and that the collected sample and the solved single crystal are the same compound.

Magnetic properties

Direct-current (dc) magnetic susceptibility measurements were recorded for **1**·2MeOH as a function of the temperature. The plot of $\chi_M T$ *vs T* is shown in Fig. 2.

At 300 K, the $\chi_M T$ value is 2.5 cm^3Kmol^{-1}, which is very close to the expected value for one isolated Yb^{3+} ion at room temperature (2.57 cm^3Kmol^{-1}). This experimental curve continuously decreases until 2 K, reaching a $\chi_M T$ value of 1.6 cm^3Kmol^{-1}. This drop in the curve can be mainly ascribed to the thermal depopulation of the excited M_J sublevels, and to the presence of significant single ion anisotropy. This latter is also confirmed by the dependence of magnetization with the field (0 to 70 kOe) at 2 K. The reduced magnetization tends to 1.65 $N\mu_B$ (Fig. 2 inset) at the maximum applied field of 70 kOe, which is significantly lower than the expected value of 4 $N\mu_B$ for one isolated Yb^{III} ion, thus also indicating the existence of magnetic anisotropy. This magnetic anisotropy is likewise confirmed by the not superimposed magnetization *versus H* curves (Fig. 2, inset) in the temperature range 2-7 K.

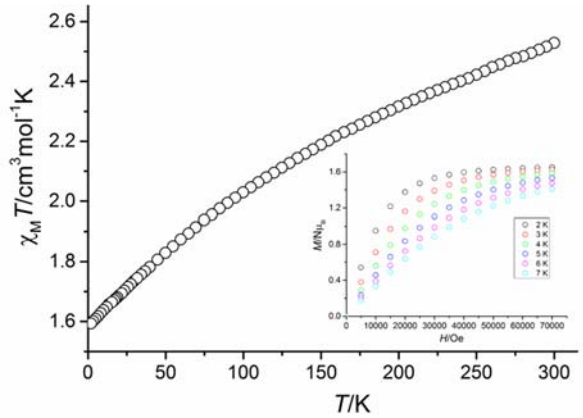

Fig. 2. $\chi_M T$ *vs T* for **1**·2MeOH under H_{dc} = 1000 Oe. Inset: $M/N\mu_B$ *vs H* in the temperature range 2-7 K.

To probe the magnetization relaxation dynamics of **1**·2MeOH, ac susceptibility measurements in the absence of an applied dc field were recorded, but **1**·2MeOH does not show peaks for out-of-phase susceptibility (χ''_M) above 2 K. This can be due to quantum tunnelling (QTM) relaxation processes,[26] which prevent to observe the SMM behaviour. Accordingly, attempts were made to suppress this quantum tunnelling with the application of a small static magnetic field.

The optimum field of 1600 Oe (Fig. S3) was determined, and, therefore, new ac data for **1**·2MeOH were recorded under this dc field. In these conditions, **1**·2MeOH shows frequency and temperature-dependence of the in phase (Fig. S4) and out-of-phase (Fig. 3) susceptibility, with maxima for χ''M between 2 and 6 K, and, consequently, field-induced SMM-like behaviour.

The Arrhenius plot (Fig. 4) shows that the data deviate from linearity in the low-temperature region, but that it is linear above 4.5 K. This linearity could indicate an Orbach relaxation process. Thus, assuming that only the Orbach relaxation predominates at high temperatures (above 4.5 K), fitting this region with equation 1 affords U_{eff} = 20.9 K (14.5 cm^{-1}), with a τ_0 factor of 5.4x10^{-7} s. These parameters are not exceptional and they are within the range of those previously described for field-induced Yb SIMs (Table S4),[15-19,27-38] and they are of the same order of magnitude as those reported for the only two formerly published pentagonal bipyramidal field-induced Yb SIMs.[32]

$$\tau^{-1} = \tau_0{}^{-1} e^{-U_{eff}/k_B T} \quad (1)$$

Nevertheless, the linearity of the Arrhenius curve is only observed in a small temperature range, and consequently, more relaxation processes must be present. The Cole–Cole plot between 2 and 6 K (Fig. S5), which displays semicircular shapes with α parameters in the range 0.15-0.10, also suggests more than one relaxation pathway. Accordingly, several models were tried in order to fit the relaxation times in the whole temperature range. These models took into account all the possible relaxation processes. It must be said that incorporating the term accounting for Orbach relaxation failed to yield a good fit. This suggests that the spin-lattice relaxation is not of the Orbach type. Hence, the Orbach relaxation seems irrelevant and should be excluded. Besides, Fig. 3 and S4 also indicate that the QTM has been suppressed at 1600 Oe, and, consequently, fittings including the QTM relaxation also failed

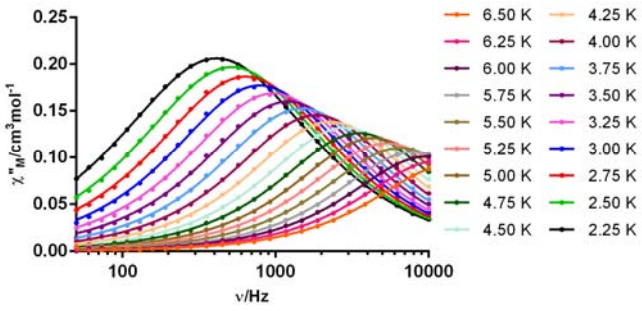

Fig. 3. Frequency dependence of χ''_M for **1**·2MeOH (H_{ac} = 10 Oe) in a dc applied field of 1600 Oe at different temperatures.

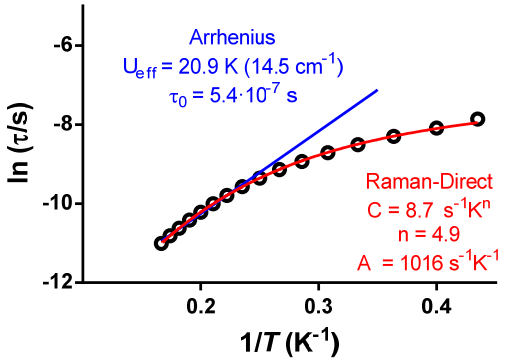

Fig. 4. Arrhenius plot for **1**·2MeOH in H_{dc} of 1600 Oe. The solid lines accounts for the best fit considering different relaxation processes.

to reproduce the curve. Thus, the best fit of the data was obtained with equation 2, which takes into account Raman and Direct processes.

$$\tau^{-1} = AT + CT^n \quad (2)$$

This fit yields the values A = 1016 $s^{-1}K^{-1}$, C = 8.7 $s^{-1}K^{-n}$ and n = 4.9. These values are also similar to those reported for Yb SIMs.[17,30,32] Even though, the n value could seem quite low because, in general, n = 7 for non-Kramers ions and n = 9 for Kramers ions. Nevertheless, when optical and acoustic phonons are taken into consideration, depending on the structure of energy levels, values of n ranging from 1 to 6 are reasonable.[39] In fact, n values as low as 2.1 have been reported for Yb field-induced SIMs,[27] and n values of 3.6 and 5.6 have been published for the only two mononuclear ytterbium field-induced single ion magnets with pentagonal bipyramidal geometry.[32]

Besides, the energy barrier between the ground and first excited state was also calculated by spectroscopic and ab initio studies (*vide infra*), and these studies also rule out the thermally activated Orbach relaxation pathway. The significant discrepancy between the energy barrier determined from ac measurements, using the Orbach model (14.5 cm^{-1}), from spectroscopic evidence (243 cm^{-1} for **1**.1 and 314 cm^{-1} for **1**.2), and from ab initio calculations (*ca*. 395 cm^{1}) gives more confidence in a combination of direct and Raman processes, and excludes an Orbach process. As it can be observed in Fig. S6, the Raman is by far the predominant relaxation process at high temperature (in the 3.5-7 K), while the direct process governs the relaxation of **1**·2MeOH below 3 K. Accordingly, this work contributes to understanding the magnetic relaxation mechanisms in the scarcely related Yb-based pentagonal bipyramidal field-induced SIMs.

Luminescence studies

Fig. 5 illustrates the low-temperature emission spectrum of **1**·2MeOH revealing the $^2F_{5/2}\rightarrow{}^2F_{7/2}$ transition ascribed to the presence of the Yb^{3+} ions. The lifetime value is below 0.02 ms, as pointed by time resolved spectroscopy (Fig. S7). Given the relevance of the emission spectrum for elucidating the magnetic anisotropy of Yb^{3+} ions, this transition was fitted using a sum of Gaussian components, using the following rational. The presence of (*R*,*S*,*R*) and (*S*,*R*,*S*) enantiomers in the asymmetric unit indicates the Yb^{3+} ions occupy two independent local coordination sites (Fig. 1) with low-symmetry, thus the splitting of the electronic levels into the maximum number of allowed components to (2*J*+1)/2 Kramers doublets is expected for each enantiomer, leading to 6 and 8 components for $^2F_{5/2}$ and $^2F_{7/2}$, respectively.

We notice that the presence of ''hot bands'' arising from the thermally populated high-energy Kramers doublets of the $^2F_{5/2}$ level were neglected. This is a feasible situation since the energy difference between the first doublet and the second one is reported to be between 300-400 cm^{-1},[17,40] and 630 cm^{-1}.[41] Thus, at 11±2 K, the probability that the first crystal field Kramers doublet is populated is negligible, considering a classical Boltzmann distribution. This rational was behind the proposed 8-fit components (identified as 1-4 and 1'-4' for the Yb^{3+}-local site of **1**.1. and 1.**2**, respectively, Fig. 5), using Gaussian functions, whose energy was constrained by careful analysis of the spectrum considering the experimental error (±5 cm^{-1}) and the full width at half-maximum (fwhm) and relative intensity were free to vary (Table S5).

The luminescence spectrum gives the first excited doublet at 243 cm^{-1} for **1**.1 and at 314 cm^{-1} for **1**.2 upon the ground-state (Fig. 5 and Tables S5, S6), an energy barrier that is within the range of those calculated for the scarcely reported mononuclear Yb SIMs spectroscopically analysed (Table 2). In addition, the significant difference of the energy barrier determined from the ac measurements, with respect to luminescence calculations, indicates that the Orbach process can be discarded in favor of a combination of direct and Raman process, as suggested for **1**·2MeOH based on the ac magnetic study.

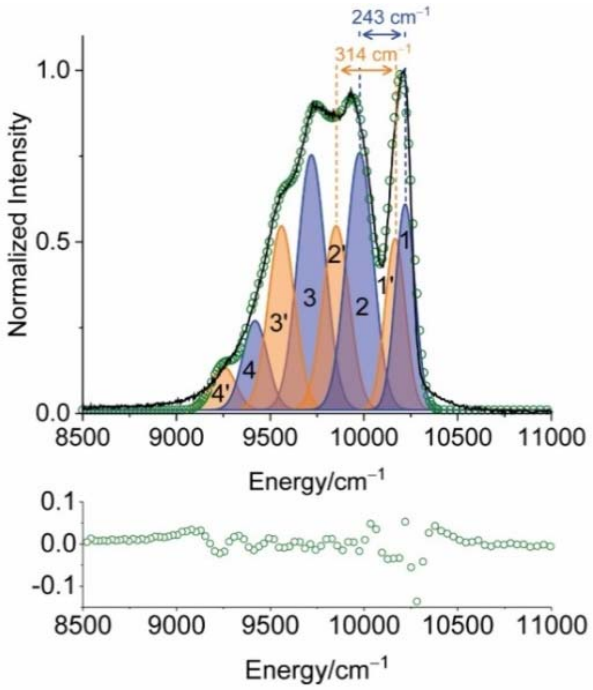

Fig. 5. Emission spectrum (acquired at 11 K, excited at 360 nm) in the region of the $^2F_{5/2}\rightarrow{}^2F_{7/2}$ transition. Multi-Gaussian functions envelop fit (open circles) and the components (orange/blue shadow Gaussians) arising from the first $^2F_{5/2}$ Stark sublevel to the $^2F_{7/2}$ multiplet. The fit regular residual plot (r^2>0.99) is shown in the bottom.

Table 2. Related luminescent mononuclear field induced-Yb-SIMs.

Yb-SMM[a]	U_{eff} / K[b]	*H* / Oe	U_{eff} / K[c]	*Environment / Geometry*	Ref.
[Yb(murex)$_3$]	15.6	2000	73	N_3O_6 /spherical capped square antiprism	15
[Yb(tta)$_3$(L^3)]	21	1000	336.7	O_8 /square antiprism	16
[Yb(trensal)]	54.67	2000	667.6	N_4O_3 /capped trigonal prism	17
[Yb(L^5)$_3$]	11.7	1000	nd	N_9 /spherical capped square antiprism	18
[Yb(depma)$_2$(H$_2$O)$_6$]Cl$_3$	28.9	750	nd	N_2O_6 /triangular dodecahedron	19

[a] Empirical formulas without solvates. [b] From ac magnetic measurements. [c] From luminescence measurements. murex = murexide; tta$^-$ = 2-thenoyltrifluoroacetonate anion; L^3 = 4,5-ethylendioxy-4′,5′-bis(2-pyridyl-N-oxidemethylthio)tetrathiafulvalene; H$_3$trensal = 2,2′,2″-tris(salicylideneimino)triethylamine; (L^5)$^-$ anion of 2 (tetrazol-5-yl)-1,10-phenanthroline; depma = 9-diethylphosphonomethylanthracene. nd = not described.

Thermometric characterization

The thermometric behaviour of **1**·2MeOH was studied by recording the emission spectra from 11 to 300 K, as shown in Fig. 6A.

The relative intensity between the Kramers doublets of the emission spectra depends on the temperature, and a thermometric parameter (Δ) is defined as

$$\Delta = \frac{I_1}{I_2} \qquad (3)$$

where I_1 and I_2 correspond to the integrated intensity of the spectra between 8500-10080 cm^{-1} and 10080-11000 cm^{-1} (marked with dashed lines in Fig. 6A), respectively. I_1 and I_2 are shown in Fig. S8. The Δ values decrease linearly as the temperature decreases between 300 and 25 K. The dependence of Δ on the temperature can be described by the empirical equation

$$\Delta = (-41 \pm 1) \times 10^{-4} T + (402 \pm 3) \times 10^{-2} \qquad (4)$$

as shown in Fig. 6B.

The performance of the thermometer was evaluated by calculating the relative sensibility (Fig. 6C)

$$S_r = \frac{1}{\Delta}\left|\frac{\partial \Delta}{\partial T}\right| \qquad (5)$$

A maximum S_r value of ≈ 0.15 %.K^{-1} is achieved at 300 K. The minimum temperature uncertainty is defined as:

$$\delta T = \frac{1}{S_r}\left|\frac{\delta \Delta}{\Delta}\right| \qquad (6)$$

where $\frac{\delta \Delta}{\Delta}$ is the relative uncertainty in Δ, considering equation S1.

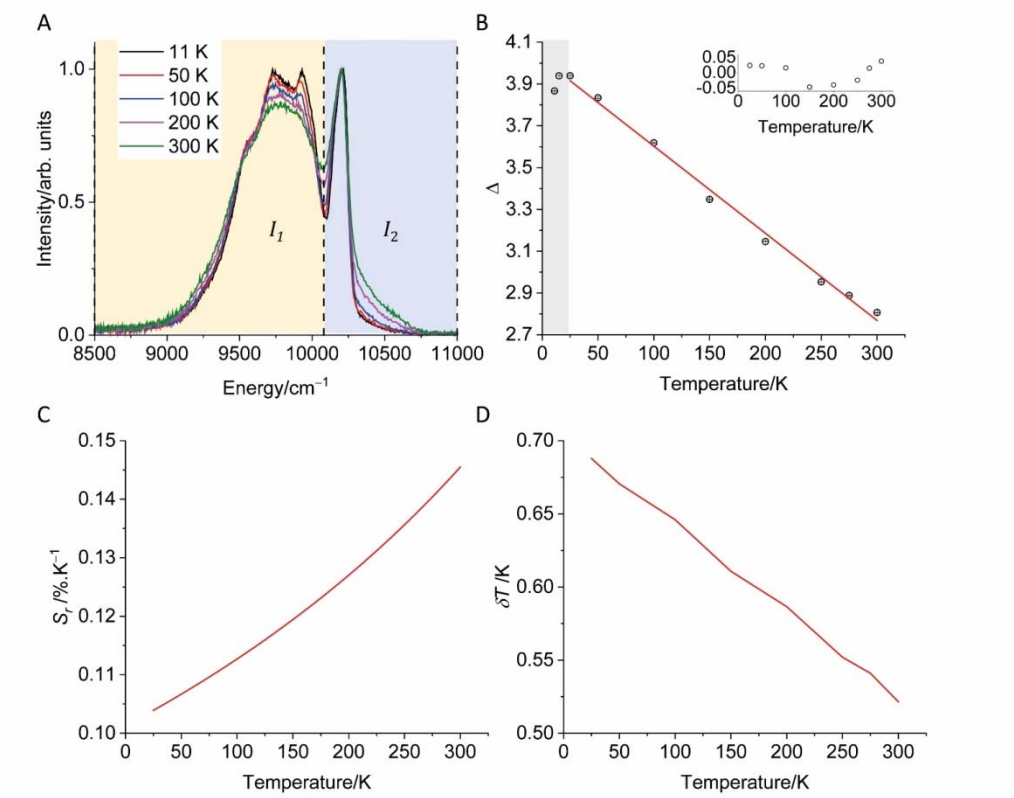

Figure 6. A) Emission spectra for selected temperatures. B) Thermometric parameter value as a function of the temperature. The line represents the best fit (r^2>0.99) to a linear function. The fit regular residual plot is shown in the inset. The shadowed area marks the region in which the thermometric parameter changes within the error meaning that for these temperatures the thermometer is out of the so-called operating range. Relative thermal sensitivity (C) and temperature uncertainty (D).

δT (Fig. 6D) is always lower than 0.7 K within operation range 25-300 K. The values found for S_r and δT are in the same order of magnitude than the previously found for the only example reported for a homonuclear single-molecule magnet Yb-based complex that can operate as thermometer.[20] And, as in the previous complex, **1**·2MeOH can function as luminescence thermometer or field-induced magnet at different temperatures but, in spite of this, **1**·2MeOH adds a new example to the poorly explored field of luminescence thermometer SMMs.

Ab initio calculations

In order to gain further insights into the magnetic anisotropy of the complexes and the magnetic relaxation pathways, we have performed complete-active-space selfconsistent field (CASSCF)[42] calculation on the basis of the single-crystal X-ray determined geometry using OPENMOLCAS.[43]

The calculated electronic structures for both **1**.1 and **1**.2 enantiomers are similar, with energy differences no greater than 20 cm^{-1}, and in reasonable agreement with the state energies deduced from the luminescence studies (Table S6). Furthermore, the ground states are found to be around 95% ±|7/2> (Table S7), which is in agreement with the obtained easy axis anisotropy of the g-tensor due to the prolate shape of the electron density of this state for Yb^{III}.[44] For **1**.1, $g_x = 0.375$, $g_y = 0.752$ and $g_z = 7.582$, while for **1**.2, $g_x = 0.310$, $g_y = 0.644$ and $g_z = 7.605$. In both complexes, the orientation of the main magnetic axes of the ground Kramers doublets is almost collinear with one of Yb-N bonds that forms the pentagon of the pentagonal bipyramid Yb^{III} center, and perpendicular to the plane formed by the three O atoms (Fig. 7 and Fig. S9). This direction of the magnetic axis allows the stabilization of the prolate shape electron density distribution of the ±|7/2> ground state, with the negatively charged atoms in a perpendicular position.

The predicted magnetic relaxation pathway, based in the averaged absolute value of the transverse magnetic moments between states, for both **1.**1 (Fig. 8) and **1.**2 (Fig. S10), shows that QTM *via* ground states is an efficient mechanism. This agrees with the absence of slow relaxation of the magnetization at zero-field. Experimentally, this QTM is quenched when a dc field is applied, leading to the observed slow relaxation of the magnetization.

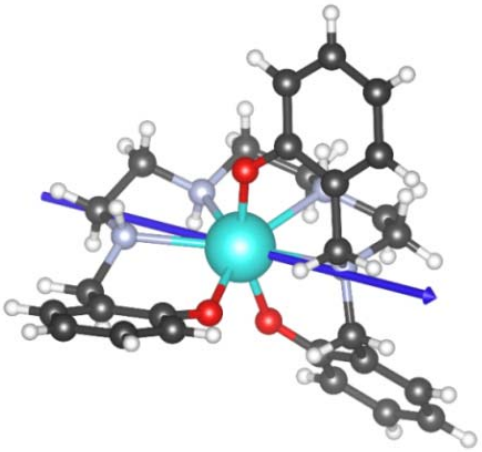

Fig. 7. The orientation of the main magnetic axis (Z) of the ground Kramers doublet on Yb^{III} for **1**.1.

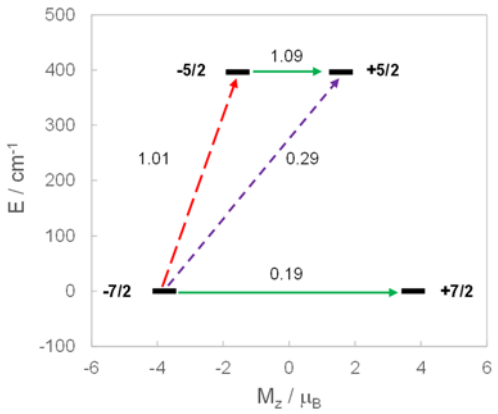

Fig. 8. Estimation of the probability for different relaxation mechanisms of the spin between the two lowest energy KDs (black lines) in 1.1: QTM and TA-QTM (green arrows); spin-phonon relaxation pathways (red and purple arrows). The values close to the arrows indicate the matrix elements of the transition magnetic moments.[45] When this value is above 0.1 an efficient spin relaxation mechanism is expected.

The calculated energy barrier for the Orbach process is *ca*. 395 cm^{-1}, in quite good agreement with the spectroscopic results, and very far away from the value of 14.5 cm^{-1} calculated from ac measurements. Accordingly, the ab initio studies support the spectroscopic studies, and they also explain the magnetic results: the QTM prevents the observation of SIM behaviour at zero field, and the calculations also suggest that the Orbach process can be discarded in favor of a combination of Raman and direct processes.

Conclusions

The opto-magnetic properties of a mononuclear Yb^{III} complex have been experimentally and theoretically analysed. These studies demonstrate that complex **1**·2MeOH shows field-induced slow relaxation of the magnetization, and Yb^{3+}-centred NIR fluorescence dependent on temperature. Accordingly, and as far as we know, **1**·2MeOH is the first mononuclear Yb field-induced single molecule magnet luminescence thermometer. The computational studies completely support the magnetic and spectroscopic results. Consequently, ab initio calculations give further insights into the magnetic dynamics of the Yb^{III} complex, explaining the existence of QTM in the absence of a magnetic field, and corroborating that the relaxation process does not take place through the first excited doublet state but through a predominant Raman relaxation pathway. Therefore, this study also contributes to increasing the knowledge in the relaxation mechanism of the scarcely explored pentagonal bipyramidal Yb-based field induced SIMs. Thus, this work add a new example to the barely investigated field of SMM luminescence thermometry, at the same time that it deepens in the magnetic relaxation pathways of uncommon pentagonal bipyramidal Yb SIMs.

Conflicts of interest

There are no conflicts to declare.

Acknowledgements

Authors thank the Spanish Ministerio de Innovación, Ciencia y Universidades (PGC2018 102052-B-C21), and the Portuguese Foundation for Science and Technology/MCTES (UIDB/50011/2020 & UIDP/50011/20) for financial support. J.C.V thanks Xunta de Galicia for his Ph.D. fellowship.

Experimental

Materials and general methods

All chemical reagents were purchased from commercial sources, and used as received without further purification. Elemental analyses of C, H and N were performed on a Carlo Erba EA 1108 analyser. ^{1}H NMR spectrum was recorded on a Bruker DPX-250 spectrometer.

Synthesis

The ligand used in this work was obtained from reduction of the previously prepared H_3L Schiff base (Scheme 1),[46] using a variation of a reported.[22] As indicated in Scheme 1, the resulting crude product is composed by a mixture of $H_6L_r^{1,2,4}$ and $H_6L_r^{1,1,4}$, according to its characterisation by ^{1}H NMR spectroscopy, which comes from a mixture of $H_6L^{1,2,4}$ and $H_6L^{1,1,4}$ by treatment with acetone. This mixture was obtained as follow: to a suspension of previously prepared H_3L (5.92 g, 12.92 mmol) in methanol (25 mL), sodium borohydride (2.05 g, 45.22 mmol) was added in small portions over a 30 min period, leading to the gradual dissolution of the Schiff base. The obtained solution was stirred at room temperature for 30 min, and then filtered. The solution was rotatory-evaporated until dryness, and the residue obtained was dissolved in a 50 mL saturated aqueous solution of ammonium acetate. This mixture was extracted with chloroform (3 x 100 mL). The corresponding organic fractions were combined and dried over anhydrous magnesium sulphate, and then this suspension was filtered. Concentration of the resulting solution led to an oily product, which was converted into a pale yellow solid by trituration with acetone, to give a mixture of $H_6L_r^{1,2,4}$ and $H_6L_r^{1,1,4}$. ^{1}H-RMN ($CDCl_3$, 250 MHz, δ in ppm): 7.22-6.70 (m, phenyl); 4.1-3.1 (various singlets, benzyl CH_2), 2.98-2.60 (m, NCH2CH2N); 1.25-1.18 (three singlets, CH_3).

[Yb($H_3L^{1,1,4}$)]·2MeOH (1·2MeOH**).** A solution of NaOH (0.069 g, 1.713 mmol) in methanol (15 mL) was added to a solution of a mixture of $H_6L_r^{1,2,4}$ and $H_6L_r^{1,1,4}$ (0.287 g, 0.571 mmol) in chloroform (20 mL). The resulting solution was mixed with a previously prepared solution of $Yb(OAc)_3$ (0.200 g, 0.571 mmol) in methanol (20 mL). The resultant solution was stirred at room temperature for 4 h, and subsequently concentrated up to 1/3 of its volume. This concentrated solution was kept in the fridge for 4 days until single crystals of [Yb($H_3L^{1,1,4}$)]·2MeOH (**1**·2MeOH), suitable for X-ray diffraction studies, appeared. The crystals were filtered, washed with diethylether and dried in an oven. Yield: 0.195 (49%). M.W.: 698.70. Anal. calcd. for $C_{29}H_{41}YbN_8O_9$: C 49.80, N 8.01, H 5.87 %: Found: C 49.47, N 7.91, H 5.82 %.

Thermogravimetrical analysis

The TGA measurements were performed using a Setsys Evolution 1750 from Setaram with a Type S sensor under N_2 environment at a heating rate of 10 ºC/min from 23 to 800 ºC.

Crystallographic refinement and structure solution

Crystal data and details of refinement are given in Table S2. Single crystals of **1**·2MeOH were obtained as detailed above. Data were collected at 100 K on a Bruker D8 VENTURE PHOTON III-14 diffractometer, employing graphite monochromatised Mo-kα (λ = 0.71073 Å) radiation. Multi-scan absorption corrections were applied using SADABS.[47] The structure was solved by standard direct methods, employing SHELXT,[48] and then refined by full matrix least-squares techniques on F^2, using SHELXL from the program package SHELX-2018.[48] All non-hydrogen atoms were anisotropically refined. Hydrogen atoms were typically included in the structure factor calculations in geometrically idealised positions. Hydrogen atoms attached to nitrogen atoms were mostly located in the corresponding Fourier map, with the intention of revealing the hydrogen bonding scheme. In this case either they were refined with thermal parameters derived from the parent atoms.

Powder X-ray diffraction studies

The powder diffractogram of **1** was recorded in a Philips diffractometer with a control unity type "PW1710", a vertical goniometer type "PW1820/00" and a generator type "Enraf Nonius FR590", operating at 40 kV and 30 mA, using monochromatised Cu-Kα (λ = 1.5418 Å) radiation. A scan was performed in the range $2 < 2\vartheta < 30°$ with t = 3 s and $\Delta 2\vartheta = 0.02°$. LeBail refinement was obtained with the aid of HighScore Plus Version 3.0d.

Magnetic measurements

Magnetic susceptibility dc and ac measurements for a powder crystalline sample of **1**·2MeOH were carried out with a PPMS Quantum Design susceptometer. The dc magnetic susceptibility data were recorded under a magnetic field of 1000 Oe in the range 2-250 K. Magnetization measurements at 2.0 K were recorded under magnetic fields ranging from 0 to 70000 Oe. Diamagnetic corrections were estimated from Pascal's Tables. Alternating current (ac) susceptibility measurements in an applied external field of 1600 Oe were performed with an oscillating ac field of 10 Oe and ac frequencies ranging from 50 to 10000 Hz.

Luminescence measurements

The photoluminescence spectra in the NIR spectral range were recorded with a modular double grating excitation spectrofluorimeter with a TRIAX 320 emission monochromator (Fluorolog-3, Horiba Scientific) coupled to a H9170 Hamamatsu photomultipliers, using a front face acquisition mode. The excitation source was a 450 W Xe arc lamp. Time-resolved measurements were performed using a pulsed Xe–Hg lamp (6 µs pulse at half width and 20–30 µs tail). The temperature was varied using a helium-closed cycle cryostat, a vacuum system (4×10^{-4} Pa), and an autotuning temperature controller (Lakeshore 330, Lakeshore) with a resistance heater. All the measurements began at least 300 s after temperature indicated in the temperature controller remained constant, thus ensuring the thermalization of the samples and constant temperature during the measurement. The conversion from wavelength to energy units and the Jacobian transformation of the intensity values were performed.[49]

Computational details

Electronic structure calculations were performed on the X-ray structures using the restricted active space self-consistent field (RASSCF)[42] method with the OPENMOLCAS code.[43] The spin-orbit coupling effect was considered perturbatively by using the restricted active space state interaction method (RASSI).[50] The ANO-RCC[51-53] basis set was used employing TZV level contractions for all the atoms: Yb {8s7p4d3f2g}, C, N y O {4s3p2d1f}, H {2s1p}. A (13,7) active space was used for both Yb^{III} centers. The SINGLE_ANISO code included in OPENMOLCAS allow us to calculate the magnetic properties of our complex as the magnetization, susceptibility, crystal field of the Yb^{III}, g-tensor and also to compute an estimation of the most probable relaxation path for the relaxation of the magnetization based on the matrix elements of the transition magnetic moments.

References

1 Molecular magnetic materials: concepts and applications, Editors: Sieklucka, B.; Pinkowicz, D. Wiley-VCH, 2017.

2 N. Ishikawa, M. Sugita, T. Ishikawa, S. Koshihara and Y. Kaizu, Lanthanide double-decker complexes functioning as magnets at the single-molecular level, *J. Am. Chem. Soc.*, 2003, **125**, 8694–8695.

3 J.-C.G. Bunzli and C. Piguet, Taking advantage of luminescent lanthanide ions, *Chem. Soc. Rev*., 2005, **34**, 1048–1077.

4 S. K. Gupta and R. Murugavel, Enriching lanthanide single-ion magnetism through symmetry and axiality, *Chem. Commun*., 2018, **54**, 3685-3696.

5 a) A. Dey, P. Kalita and V. Chandrasekhar, Lanthanide(III)-Based Single-Ion Magnets, *ACS Omega*, 2018, **3**, 9462−9475; b) A. K. Bar, P. Kalita, M. K. Singh, G. Rajaraman and V. Chandrasekhar, Low-coordinate mononuclear lanthanide complexes as molecular nanomagnets, *Coord. Chem. Rev*., 2018, **367**, 163–216.

6 Z. Zhu, M. Guo, X-L. Li and J. Tang, Molecular magnetism of lanthanide: advances and perspectives, *Coord. Chem. Rev*., 2019, **378**, 350–364.

7 F.-S. Guo, B. M. Day, Y.-C. Chen, M.-L. Tong, A. Mansikkamäki and R. A. Layfield, Magnetic hysteresis up to 80 kelvin in a dysprosium metallocene single-molecule magnet, *Science*, 2018, **362**, 1400-1403

8 J. Long, Y. Guari, R. A.S. Ferreira, L. D. Carlos and J. Larionova, Recent advances in luminescent lanthanide based single-molecule magnets, *Coord. Chem. Rev*., 2018, **363**, 57–70.

9 J-H. Jia, Q-W. Li, Y-C. Chen, J-L. Liu and M-L. Tong, Luminescent single-molecule magnets based on lanthanides: design strategies, recent advances and magneto-luminescent studies, *Coord. Chem. Rev*., 2019, **378**, 365-381.

10 Y. Bi, X.-T. Wang, W. Liao, X. Wang, R. Deng, H. Zhang and S. Gao, Thiacalix[4]arene-supported planar Ln_4 (Ln = Tb^{III}, Dy^{III}) clusters: toward luminescent and magnetic bifunctional materials, *Inorg. Chem*., 2009, **48**, 11743–11747.

11 G. Cucinotta, M. Perfetti, J. Luzon, M. Etienne, P.-E. Car, A. Caneschi, G. Calvez, K. Bernot and R. Sessoli, Magnetic anisotropy in a dysprosium/DOTA single-molecule magnet: beyond simple magneto-structural correlations *Angew. Chem. Int. Ed.,* 2012, **51**, 1606–1610.

12 Y. Bi, C. Chen, Y.-F. Zhao, Y.-Q. Zhang, S.-D. Jiang, B.-W. Wang, J.-B. Han, J.-L. Sun, Z.-Q. Bian, Z.-M. Wang and S. Gao, Thermostability and photoluminescence of Dy(iii) single-molecule magnets under a magnetic field, *Chem. Sci*., 2016, **7**, 5020–5031.

13 (a) E. Chelebaeva, J. Larionova, Y. Guari, R. A. S. Ferreira, Luis D. Carlos, F. A. Almeida-Paz, A. Trifonov and C. Guérin, luminescent and magnetic cyano-bridged coordination polymers containing 4d−4f ions: toward multifunctional materials, *Inorg. Chem*., 2009, **48**, 5983–5995. (b) E. Chelebaeva, J. Long, J. Larionova, R. A. S. Ferreira, Luis D. Carlos, F. A. Almeida-Paz, J. B. R. Gomes, A. Trifonov, C. Guérin and Y. Guari, Bifunctional mixed-lanthanide cyano-bridged coordination polymers $Ln_{0.5}Ln'_{0.5}(H_2O)_5[W(CN)_8]$ (Ln/Ln′ = Eu^{3+}/Tb^{3+}, Eu^{3+}/Gd^{3+}, Tb^{3+}/Sm^{3+}), Inorg. Chem., 2012, **51**, 9005-9016.

14 X. Feng, Y. Shang, H. Zhang, R. Li, W. Wang, D. Zhang, L. Wang and Z. Li, Enhanced luminescence and tunable magnetic properties of lanthanide coordination polymers based on fluorine substitution and phenanthroline ligand, *RSC Adv*., 2019, **9**, 16328-16338.

15 X. Yi, K. Bernot, V. Le Corre, G. Calvez, F. Pointillart, O. Cador, B. Le Guennic, J. Jung, O. Maury, V. Placide, Y. Guyot, T. Roisnel, C. Daiguebonne and O. Guillou, Unraveling the crystal structure of lanthanide–murexide complexes: use of an ancient complexometry indicator as a near-infrared-emitting single-ion magnet, *Chem. Eur. J*. 2014, **20**, 1569-1576.

16 K. Soussi, J. Jung, F. Pointillart, B. Le Guennic, B. Lefeuvre, S. Golhen, O. Cador, Y. Guyot, O. Maury and L. Ouahab, Magnetic and photo-physical investigations into Dy^{III} and Yb^{III} complexes involving tetrathiafulvalene ligand, *Inorg. Chem. Front.,* 2015, **2**, 1105-1117.

17 K.S. Pedersen, J. Dreiser, H. Weihe, R. Sibille, H.V. Johannesen, M.A. Sorensen, B.E. Nielsen, M. Sigrist, H. Mutka, S. Rols, J. Bendix and S. Piligkos, Design of single-molecule magnets: insufficiency of the anisotropy barrier as the sole criterion, *Inorg. Chem*., 2015, **54**, 7600-7606.

18 J-R. Jiménez, I. F. Díaz-Ortega, E. Ruiz, D. Aravena, S. J. A. Pope, E. Colacio and J. M. Herrera, Lanthanide tetrazolate complexes combining single-molecule magnet and luminescence properties: the effect of the replacement of tetrazolate N_3 by β-diketonate ligands on the anisotropy energy barrier *Chem. Eur. J*., 2016, **22**, 14548–14559.

19 Q. Zou, X-D. Huang, J-C. Liu, S-S. Bao and L-M. Zheng, Lanthanide anthracene complexes: slow magnetic relaxation and luminescence in Dy^{III}, Er^{III} and Yb^{III} based materials, *Dalton Trans*., 2019, **48**, 2735-2740.

20 G. Brunet, R. Marin, M-J. Monk, R-G. Diogo, A. Gálico, F. A. Sigoli, E. A. Suturina, E. Hemmer and M. Murugesu, Exploring the dual functionality of an ytterbium complex for luminescence thermmetry and slow magnetic relaxation. *Chem. Sci*., 2019, **10**, 6799-6808.

21 (a) M. Fondo, J. Corredoira-Vázquez, A. M. García-Deibe, J Sanmartín-Matalobos, J. M. Herrera and E. Colacio, *Inorg. Chem*., 2017, **56**, 5646-5656. (b) M. Fondo, J. Corredoira-

Vázquez, A. Herrera-Lanzós, A. M. García-Deibe, J Sanmartín-Matalobos, J. M. Herrera, E. Colacio and C. Nuñez, *Dalton Trans*., 2017, **46**, 17000–17009. (c) M. Fondo, J. Corredoira-Vázquez, A. M. García-Deibe, J Sanmartín-Matalobos, J. M. Herrera and E. Colacio, *Inorg. Chem.*, 2018, **57**, 10100–10110. (d) M. Fondo, J. Corredoira-Vázquez, A. M. García-Deibe, S. Gómez-Coca, E. Ruiz, J. Sanmartín, *Dalton Trans*., 2020, **49**, 8389-8401.

22 L-W. Yang, S. Liu, E. Wong, S. J. Rettig and C. Orvig, Complexes of trivalent metal ions with potentially heptadentate N_4O_3 Schiff base and amine phenol ligands of varying rigidity, *Inorg. Chem*. **1995**, *34*, 2164-2178.

23 H. D. Flack, On enantiomorph-polarity estimation, *Acta Crystallogr., Sect. A*, 1983, **39**, 876-881.

24 P. G. Jones, The determination of absolute structure. III. An ambiguity table for the non-centrosymmetric crystal classes, *Acta Crystallogr., Sect. A*, 1986, **42**, 57.

25 (a) M. Llunell, D. Casanova, J. Cirera, J. M. Bofill, P. Alemany, S. Alvarez, M. Pinsky and D. D. Avnir, SHAPE v1.1b, Barcelona, 2005; (b) A. Ruiz-Martínez, D. Casanova and S. Alvarez, Polyhedral structures with an odd number of vertices: nine-coordinate metal compounds, *Chem. Eur. J*., 2008, **14**, 1291–1303; (c) M. Llunell, D. Casanova, J. Cirera, P. Alemany and S. Alvarez, SHAPE: Program for the stereochemical analysis of molecular fragments by means of continuous shape measures and associated tools; University of Barcelona, Barcelona, Spain, 2010.

26 (a) J. R. Friedman, M. P. Sarachick, J. Tejada and R. Ziolo, Macroscopic measurement of resonant magnetization tunneling in high-spin molecules, *Phys. Rev. Lett*., 1996, **76**, 3830–3833; (b) L. Thomas, F. Lionti, R. Ballou, D. Gatteschi, R. Sessoli and B. Barbara, Macroscopic quantum tunneling of magnetization in a single crystal of nanomagnets, *Nature*, 1996, **383**, 145–147.

27 J-L. Liu, K. Yuan, J-D. Leng, L. Ungur, W. Wernsdorfer, F-S. Guo, L. F. Chibotaru and M-L. Tong, A six-coordinate ytterbium complex exhibiting easy-plane anisotropy and field-induced single-ion magnet behaviour, *Inorg. Chem*., 2012, **51**, 8538−8544.

28 M. E. Boulon, G. Cucinotta, J. Luzon, C. Degl'Innocenti, M. Perfetti, K. Bernot, G. Calvez, A. Caneschi and R. Sessoli, Magnetic anisotropy and spin-parity effect along the series of lanthanide complexes with DOTA, *Angew. Chem. Int. Ed*., 2013, **52**, 350-354.

29 W. Huang, J. Xu, D. Wu, X. Huang and J. Jiang, Rhodamine-based field-induced single molecule magnets in Yb(III) and Dy(III) series, *New J. Chem*., 2015, **39**, 8650-8657.

30 A. Lannes and D. Luneau, New family of lanthanide-based complexes with different scorpionate-type ligands: a rare case where dysprosium and ytterbium analogues display single-ion-magnet behaviour, *Inorg. Chem.*, 2015, **54**, 6736−6743.

31 A. A. Trifonov, B. Shestakov, J. Long, K. Lyssenko, Y. Guari and J. Larionova, An organoytterbium(III) complex exhibiting field-induced single-ion-magnet behavior, *Inorg. Chem.*, 2015, **54**, 7667−7669.

32 A. V. Gavrikov, N. N. Efimov, Z. V. Dobrokhotova, A. B. Ilyukhin, P. N. Vasilyev and V. M. Novotortsev, Novel mononuclear Ln complexes with pyrazine-2-carboxylate and acetylacetonate co-ligands: remarkable single molecule magnet behavior of a Yb derivative, *Dalton Trans*., 2017, **46**, 11806-11816.

33 D-Q. Wu, D. Shao, X-Q. Wei, F-X. Shen, L. Shi, Y-Q. Zhang and X-Y. Wang, Single-ion magnetism in seven-coordinate Yb^{III} complexes with distorted D_{5h} coordination geometry *Dalton Trans.*, 2017, **46**, 12884-12892.

34 G. Peng, Y-Y. Zhang, B. Li, X-F. Sun, H-L. Cai, D-J. Li, Z-G. Gu and G. E. Kostakis, Single molecule magnetic behaviour in lanthanide naphthalenesulfonate complexes, *Dalton Trans*., 2018, **47**, 17349-17356.

35 W. Zhao, H. Cui, X-Y. Chen, G. Yi, L. Chen, A. Yuan and C-L. Luo, An eight-coordinate ytterbium complex with a hexagonal bipyramid geometry exhibiting field induced single-ion magnet behaviour, *Dalton Trans*., 2019, **48**, 5621-5626.

36 Gorczyński, D. Marcinkowski, M. Kubicki, M. Loffler, M. Korabik, M. Karbowiak, P. Wiśniewski, C. Rudowicz and V. Patroniak, New field-induced single ion magnets based on prolate Er(III) and Yb(III) ions: tuning the energy barrier Ueff by the choice of counterions within an N3-tridentate Schiff-base scaffold, *Inorg. Chem. Front.*, 2018, **5**, 605–618

37 L. Maxwell, M. Amoza and E. Ruiz, Mononuclear Lanthanide Complexes with 18-Crown‑6 Ether: Synthesis, Characterization, Magnetic Properties, and Theoretical Studies, *Inorg. Chem*., 2018, 57, 13225–13234

38 S. P. Petrosyants, K. A. Babeshkin, A. V. Gavrikov, A. B. Ilyukhin, E. V. Belova and N. N. Efimov, Towards comparative investigation of Er- and Yb-based SMMs: the effect of the coordination environment configuration on the magnetic relaxation in the series of heteroleptic thiocyanate complexes, *Dalton Trans*., 2019, **48**, 12644–12655.

39 (a) A. Singh and K. N. Shrivastava, Optical-acoustic two-phonon relaxation in spin systems, *Phys. Status Solidi* B, 1979, **95**, 273-277; (b) K. N. Shrivastava, Theory of spin–lattice relaxation, *Phys. Status Solidi* B, 1983, **117**, 437-458.

40 (a) Q-W. Li, J-L. Liu, J-H. Jia, J-D. Leng, W-Q. Lin, Y-C. Chena and M-L. Tong, Fluorescent single-ion magnets: molecular hybrid $(HNEt_3)[Dy_xYb_{1-x}(bpyda)_2]$ (x = 0.135–1), *Dalton Trans.*, 2013, **42**, 11262-11270; (b) Q-W. Li, J-L. Liu, J-H. Jia, Y-C. Chen, J. Liu, L-F. Wang and M-L. Tong, "Half-sandwich" Yb^{III} single-ion magnets with metallacrowns, *Chem. Commun*., 2015, **51**, 10291-10294.

41 G. S. Pati, Z. Warren, N. Yu, and M. S. Shahriar, Computational studies of light shift in a Raman–Ramsey interference-based atomic clock, *J. Opt. Soc. Am.* B, 2010, **27**, 388-394.

42 B. O. Roos, Accurate Calculations and Calibration. In *Lecture notes in quantum chemistry*; B. O. Roos, Ed.; Springer-Verlag: Berlin, Heidelberg, New York, 1992; p 177.

43 I. Fdez. Galván, M. Vacher, A. Alavi, C. Angeli, F. Aquilante, J. Autschbach, J. J. Bao, S. I. Bokarev, N. A. Bogdanov, R. K. Carlson, L. F. Chibotaru, J. Creutzberg, N. Dattani, M. G. Delcey, S. S. Dong, A. Dreuw, L. Freitag, L. M. Frutos, L. Gagliardi, F. Gendron, A. Giussani, L. González, G. Grell, M. Guo, C. E. Hoyer, M. Johansson, S. Keller, S. Knecht, G. Kovačević, E. Källman, G. Li Manni, M. Lundberg, Y. Ma, S. Mai, J. P. Malhado, P. A. Malmqvist, P. Marquetand, S. A. Mewes, J. Norell, M. Olivucci, M. Oppel, Q. M. Phung, K. Pierloot, F. Plasser, M. Reiher, A. M. Sand, I. Schapiro, P. Sharma, C. J. Stein, L. K. Sørensen, D. G. Truhlar, M. Ugandi, L. Ungur, A. Valentini, S. Vancoillie, V.

Veryazov, O. Weser, T. A. Wesołowski, P-O. Widmark, S. Wouters, A. Zech, J. P. Zobel, R. Lindh, OpenMolcas: from source code to insight, *J. Chem. Theor. Comput.*, 2019**, 15**, 5925-5964.

44 J. D. Rinehart and J. R. Long, Exploiting single-ion anisotropy in the design of f element single-molecule magnets, *Chem. Sci.*, 2011, **2**, 2078–2085.

45 L. Ungur and L. Chibotaru, Strategies toward high-temperature lanthanide-based single-molecule magnets, *Inorg. Chem.*, 2016, **556**, 10043-10056.

46 M. Fondo, A. M. García-Deibe, M. R. Bermejo, J. Sanmartín and A. L. Llamas-Saiz, Spontaneous carbon dioxide fixation: a μ_4-carbonate bridged tetranuclear zinc(II) complex of a heptadentate Schiff base *J. Chem. Soc., Dalton Trans.*, 2002, 4746-4750.

47 Sheldrick, G. M. *SADABS, Area-Detector Absorption Correction*; Siemens Industrial Automation, Inc.: Madison, WI, 2001.

48 G. M. Sheldrick, Crystal structure refinement with SHELXL. *Acta Cryst.*, 2015, **C71**, 3–8.

49 J. Mooney and P. Kambhampati, Get the basics right: Jacobian conversion of wavelength and energy scales for quantitative analysis of emission spectra, *J. Phys. Chem. Lett.*, 2013, **4**, 3316-3318.

50 P. Å. Malmqvist, B. O. Roos and B. Schimmelpfennig, The restricted active space (RAS) state interaction approach with spin-orbit coupling, *Chem. Phys. Lett.*, 2002, **357**, 230–240.

51 B. O. Roos, R. Lindh, P. Å. Malmqvist, V. Veryazov and P.-O. Widmark, Main group atoms and dimers studied with a new relativistic ANO basis set, *J. Phys. Chem. A*, 2004, **108**, 2851–2858.

52 P.-O. Widmark, P.-Å. Malmqvist and B. O. Roos, Density matrix averaged atomic natural orbital (ANO) basis sets for correlated molecular wave functions, *Theor. Chim. Acta*, 1990, **77**, 291–306.

53 B. O. Roos, R. Lindh, P.-Å. Malmqvist, V. Veryazov, P.-O. Widmark and A. C. Borin, New relativistic atomic natural orbital basis sets for lanthanide atoms with applications to the Ce diatom and LuF_3, *J. Phys. Chem. A*, 2008, **112**, 11431–11435.

